condensed matter

MDPI

Communication

From Phonons to Domain Walls, the Central Peak and "Critical Slowing Down"

Ekhard K. H. Salje [1] and Annette Bussmann-Holder [2,*]

[1] Department of Earth Sciences, University of Cambridge, Cambridge CB2 3EQ, UK; es10002@cam.ac.uk
[2] Max-Planck-Institute for Solid State Research, Heisenbergstr. 1, D-70569 Stuttgart, Germany
* Correspondence: a.bussmann-holder@fkf.mpg.de

Abstract: We investigate perovskite oxides from different perspectives, namely their pseudo-harmonic dynamical properties, their dynamical properties when strong anharmonicity exists, and the intriguing functionalities arising from domain walls. Taking these viewpoints together yields a rather complex picture of this material class, which has not been found in previous approaches. It opens pathways to novel applications and reveals the rich ground states beyond the fictitious belief in the 'simplicity of perovskites and such structures'.

Keywords: anharmonicity; phase transitions; domain walls; perovskite oxides

Citation: Salje, E.K.H.; Bussmann-Holder, A. From Phonons to Domain Walls, the Central Peak and "Critical Slowing Down". *Condens. Matter* **2024**, *9*, 39. https://doi.org/10.3390/condmat9040039

Academic Editor: Yoram Dagan

Received: 23 August 2024
Revised: 23 September 2024
Accepted: 27 September 2024
Published: 1 October 2024

1. Introduction

Perturbation approaches have dominated the field of phase transitions ever since the celebrated papers by Landau and Lifshitz from the late 1930s [1,2]. When Bill Cochran, in 1959 [3], first formulated the idea that parameters like temperature, pressure, chemical potential, etc., gently modify phonons, the concept of optical soft modes was born. In all displacive systems, phonons are weakly anharmonic, which leads to linear temperature dependences of the squared phonon frequency ω^2. In the high-symmetry phase, the linear ω^2 dependence is virtually always observed over relatively large temperature intervals, while phonon branches at lower temperatures split in the symmetry-broken phase. Additional anharmonicities become apparent in the symmetry-broken phase. In second-order phase transitions, as exemplified in $SrTiO_3$, an additional conundrum was discussed by Alex Müller: if the phonon frequency approaches zero, the phonon amplitude diverges [4,5]. Terms like 'critical slowing down' for motion and 'central peak' for the frequency spectrum were coined to describe this situation [6,7]—often without identifying the exact physical process that stabilizes phonons close to the transition point. Here, we describe these phenomena in simple models without resorting to DFT techniques [8] in order to emphasise the underlying physical principles in the most transparent way.

2. Pseudo-Harmonic Approach

The first theories devoted to lattice dynamics in ferroelectric perovskites can be traced back to Cochran (1961) [9], where he introduces a shell model description for ferroelectrics to account for the electronic polarizability of the ions, i.e., they are not describable as rigid ions because the relative displacements of their electronic shells with respect to the core have to be included. By using the adiabatic principle, the electronic and ionic degrees of freedom are decoupled, and the renormalized ionic model must be considered in deeper detail. In view of the discovery that in perovskite oxides, the ferroelectric phase transition is accompanied by the softening of an optic mode, the model explicitly considers anharmonicity by introducing a fourth-order term in the lattice dynamical Hamiltonian [10,11]. The linear T-dependence of the squared soft optic mode is obtained within the self-consistent phonon approximation (SPA), where the fourth-order term is replaced by its cumulant

expansion [12]. However, a closer look at the temperature evolution of ω^2 reveals that such simple dependence is not realized, neither in the limit of $\omega^2 \to 0$ nor at $T >> T_C$, where saturation of ω^2 is observed [13]. In the limit $\omega^2 \to 0$, very apparent deviations from the above law are commonly seen in quantum paraelectrics, e.g., $SrTiO_3$ [14], where saturation of the soft mode takes place due to quantum fluctuations that are larger than the original soft mode, which is related to the displacement coordinates. Both temperature regimes have been successfully described within the polarizability model [15], where anisotropic core–shell coupling at the oxygen ion is explicitly incorporated [16,17]. With respect to the rigid A ion in ABO_3, this coupling is purely harmonic. Regarding the B ion, the coupling consists of an attractive harmonic term g_2 and a stabilizing anharmonic fourth-order term g_4, which, within the SPA, is replaced by a temperature-dependent pseudo-harmonic approximation, namely $g_T = g_2 + 3g_4\langle w_T^2 \rangle$, where $\langle w_T^2 \rangle$ is the relative core–shell displacement coordinate at the oxygen ion lattice site. The Hamiltonian of the polarizability model is given by

$$H = T + V \tag{1a}$$

$$T = \sum_n \left[m_1 \dot{u}_{1n}^2 + m_2 \dot{u}_{2n}^2 + m_{el} \dot{v}_{1n}^2 \right] \tag{1b}$$

$$V = \sum_n \left[f'(u_{1n} - u_{1n-1})^2 + f(u_{2n} - w_{1n} - u_{1n})^2 + f(u_{2n+1} - w_{1n} - u_{1n})^2 + g_2 w_{1n}^2 + g_4 w_{1n}^4 \right] \tag{1c}$$

where u_{in}, v_{1n} are the displacement coordinates of ion m_i (i = 1, 2) and shell m_1 in the n-th unit cell, and $w_{1n} = v_{1n} - u_{1n}$, f and f' are nearest- and second-nearest-neighbour harmonic coupling constants. Within this approach, the lowest transverse optic and acoustic modes are well described as a function of momentum q and temperature T, where the latter is obtained through the SPA. The soft transverse q = 0 optic mode is explicitly given by $\mu\omega_{TO}^2(q = 0) = 2fg_T/(2f + g_T)$, with μ being the reduced cell mass. While the conventional approach yields the linear in T behaviour [13] for any temperature, this equation reproduces the quantum paraelectric behaviour as well as the saturation limit due to the T-dependence of the denominator (explicit consequences for quantum extensions to phase transitions were discussed in [2]). An interesting feature appears in the limit when optic and acoustic modes start to couple, which happens as a function of temperature and momentum [18–20]. In such a case, a critical momentum q_c can be defined where the modes are closest to each other. On cooling, q_c approaches zero and defines with decreasing temperature and defines real space regions that are identified with elastic anomalies and polar nanoregions. Both grow in size when approaching the phase transition temperature T_C, at which point the nano-regions coalesce into a global polar state. The onset temperature for their formation does not coincide with Burn's temperature T_B [21,22], which is notoriously difficult to determine experimentally, but occurs well below estimated values of T_B. A precursor temperature is defined where the crossover between the high-temperature saturation and the pre-transitional softening occurs. This temperature was predicted to be $T^* \approx 1.1\ T_C$. [23]. Other values, which are of the same order of magnitude, stem from molecular dynamics simulations [24] and have been discussed in Ref. [24] (between 1.01 T_c and 1.4 T_c). These temperatures have been observed experimentally in many perovskite oxides by Brillouin scattering [25], dielectric spectroscopy [26], birefringence [27], ultrasound, RUS of elastic softening [28–31] and various other techniques. Importantly, this demonstrates that a nominally displacive system always carries an order–disorder component and thereby indicates a coexistence of both classification classes [23,32]. As is evident from Equation (1c), a local double-well potential is inherently present in perovskite oxides, which stems from the oxygen ion nonlinear polarizability, which diverges as a function of its volume and is temperature-dependent [33,34].

3. Periodons and Incommensurations

In the following, the concept of soft modes is extended to nonlinear solutions where the continuum aspect of the Φ_4 model, i.e., a model based on a double-well potential [35], is complemented by discrete solutions appearing on the lattice [36]. These are relevant to systems in which local lattice distortions break the translational symmetry caused by, e.g., defects, impurities, doping or intrinsic nonlinearity. First exact nonlinear solutions are compared to SPA solutions for the case of ferroelectric non-perovskite SnTe, which is a chalcogenide where Te^{2-} exhibits a comparable role to O^{2-} in perovskite oxides [37,38]. This IV-VI semiconductor undergoes a cubic-to-rhombohedral phase transition and a ferroelectric phase at $T_C \approx 100$ K. In addition, it exhibits phonon anomalies in the various dispersion branches, which appear as a dips or kinks [37,38]. Next, the coupling between the nonlinear and SPA phonons is discussed, which leads to phase transitions at finite critical momentum $q_c \neq 0$, which is applicable to K_2SeO_4. Note that this system undergoes a paraelectric incommensurate transition at $T_i = 127$ K, and one to a truly ferroelectric one at $T_C = 96$ K. By analogy with perovskite ionic systems, this compound can also be modelled within the dipolar shell model approximation (see above). The harmonic lattice potential is given by $\varphi^{(2)} = \varphi_{ii} + \varphi_{ei} + \varphi_{ee'}$ where φ_{ii} is the ion–ion, φ_{ei} the electron–ion and $\varphi_{ee'}$ the electron–electron interaction. In analogy to the case discussed above, the electron–ion interaction potential is extended by a fourth-order anisotropic term $\varphi_{ei}^{(4)} = \frac{1}{4}\sum_{L,\alpha} g_{4,\alpha}(\kappa) w_\alpha^4(L)$, where w is the relative core–shell displacement coordinate at lattice site $L = (l, \kappa)$ and $\alpha = x, y, z$. Within the SPA, this term is replaced by $w_\alpha^3(L) = 3w_\alpha(L)\langle w_\alpha^2(L)\rangle_T$, with the bracketed term being the thermal average. While in the continuum limit, kink-type and solitary solutions exist, here, nonlinear periodic three-dimensional lattice solutions (periodons) are obtained using the ansatz for the displacements $x = u, v, w$:

$$\vec{x}(L) = Re\left\{\vec{X}_1 exp\left[i\left(\omega t - \vec{q}\vec{R}(L)\right]\right] + \vec{X}_3 exp\left[3i\left(\omega t - \vec{q}\vec{R}(L)\right]\right]\right\}, \quad (2)$$

with the amplitudes $\vec{X}_1$, $\vec{X}_3$ being determined by the equations of motion. The periodon dispersion relation is given by $\omega_p\left(\vec{q}\right) = \frac{1}{3}\omega_R\left(3\vec{q}\right)$, where $\omega_R\left(\vec{q}\right)$ is the SPA dispersion relation. In Figure 1, periodons and phonons are shown for the ferroelectric rock-salt structure IV-VI compound SnTe. By including the interaction between phonons and periodons, finite momentum soft modes are obtained, which freeze at momentum $q = q_c$. This is best exemplified for the case of a pseudo-linear model with nearest-neighbour interactions and one polarizable ion in the unit cell. This model is a simplification of the polarizability model, but it captures its essential features, namely the nonlinear polarizability of the oxygen ion. Correspondingly, its Hamiltonian is only slightly varied as compared to Equation (1):

$$H = \frac{1}{2}\sum_n \left[M_1 \dot{u}_{1n}^2 + m\dot{v}_{1n}^2 + f'(u_{1n} - u_{1n-1})^2 + f(v_{1n} - v_{1n-1})^2 + g_2 w_{1n}^2 + \frac{1}{2} g_4 w_{1n}^4\right] \quad (3)$$

where the same notations as above have been used. Since, here, only a single ion approximation is used, the index 1 is omitted in the following. The equations of motion are given by:

$$M\ddot{u}_n^2 = g_2 w_n + g_4 w_n^3 + f\prime D u_n \quad (4a)$$

$$m_e \ddot{v}_n = -g_2 w_n - g_4 w_n^3 + fD(w_n + u_n) = 0 \quad (4b)$$

where $Dx_n = x_{n+1} + x_{n-1} - 2x_n$ is the difference operator. Solutions to these equations are given by $w_n = A\sin(\omega t - nqa), u_n = B\sin(\omega t - nqa) + C\sin 3(\omega t - nqa)$ with the dispersion relation $M\omega_p^2(q) = \frac{4}{9}(f + f')\sin^2\left(\frac{3qa}{2}\right)$ and amplitudes $A^2(q) = \frac{4}{3}\left[-g_2 - M\omega_f^2\left(1 - \frac{\omega_f^2}{\omega_R^2 - \omega_p^2}\right)\right]$, with ω_f^2, ω_R^2 being the ferroelectric and rigid ion squared frequencies. The coupling between phonon and periodon is imposed by a super-

position of their displacements, namely $w_n = w_{np} + w_{ns}, u_n = u_{np} + u_{ns}$. This leads to two types of equations of motion, namely one in the periodon displacement coordinate, u_{np}, and the other in the phonon-related one, u_{ns} :

$$M\ddot{u}_{ns} = \left(f + f'\right) D u_{ns} + f D w_{ns} \tag{5a}$$

$$0 = \left[g_T + 3g_4 w_{np}^2\right] - fD[w_{ns} + u_{ns}] \tag{5b}$$

$$M\ddot{u}_{np} = \left(f + f'\right) D u_{np} + f D w_{np} \tag{5c}$$

$$0 = g_T w_{np} + g_4 w_{np}^3 - fD\left[w_{np} + u_{np}\right] \tag{5d}$$

where for w_{ns}, the SPA has been used, and g_T has been defined above. As is apparent from the above equations, the periodon amplitude adopts a temperature dependence where two regimes can be differentiated, namely the high-temperature one where SPA phonons exist in a fluctuating periodon field, whereas at low temperatures, static periodons are observed. This yields a site-dependent electron–ion coupling:

$$g_T + 3g_4 w_{np}^2\left(\frac{2\pi}{3}\right) = \left\{ \begin{matrix} g_T, \; n \equiv 0 \; (mod 3) \\ -2g_T - \frac{9}{\frac{1}{f} + \frac{1}{f'}} \end{matrix}, \; n \equiv 1 \; or \; 2 \; (mod 3) \right\} \tag{6}$$

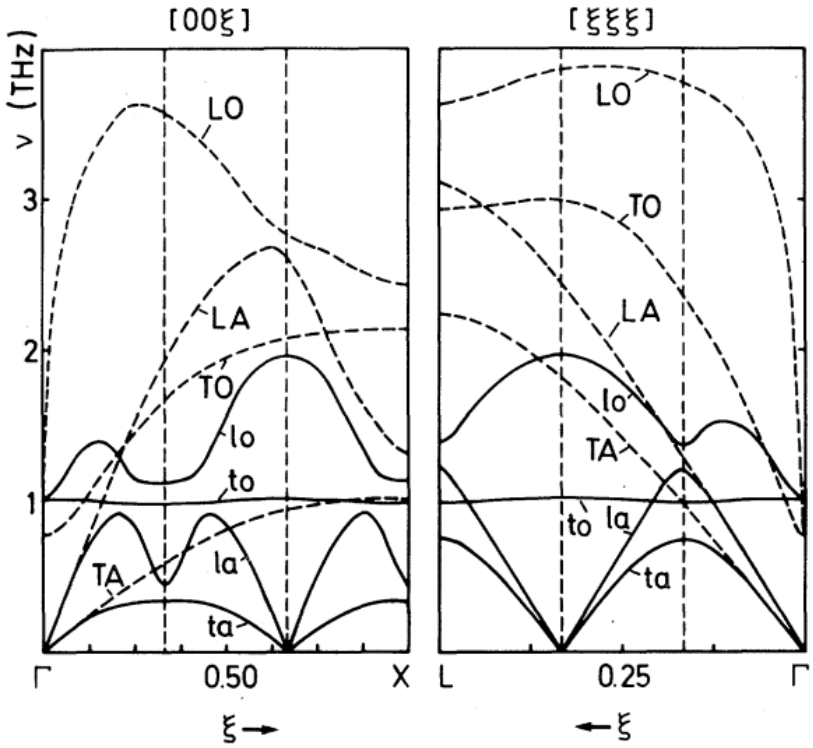

Figure 1. Dispersion curves of phonons (dashed lines) and periodons (solid lines) in SnTe at 100 K. Capital (small) letters denote the polarization of them. Parameters have been adopted from Refs. [37,38].

In Figures 2 and 3, the theoretical results for K_2SeO_4 are compared to experimental data [39,40]. The temperature dependence is given by g_T and concerns the commensurate part, whereas $f\prime(T)$ determines the incommensurate intersite elastic coupling, which shifts the minimum in the dispersion $\omega(q)$ away from the commensurate value $qa = 2\pi/3$ to higher values.

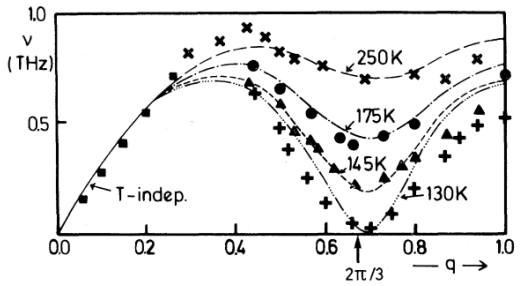

Figure 2. Dispersion of the coupled phonon–periodon mode in the paraelectric regime ($T > T_C = 127$ K) of K_2SeO_4 with $f + f' = 09.THz^2x$ mass unit. Experimental data (crosses, dots, triangles, and crosses) have been taken from Refs. [39,40].

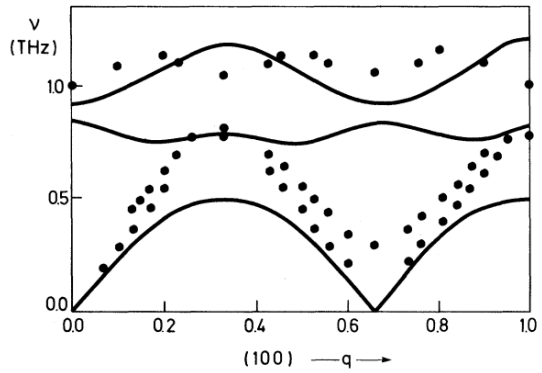

Figure 3. Tripling of the transverse acoustic coupled mode in the ferroelectric regime at T = 40 K.

Upon extrapolating g_T and $f\prime(T)$ to zero (Figure 4), it is obvious that the former governs the second-order phase transition at $T_i = 127$ K, while the latter determines the lock-in transition at $T_C = 93$ K. Reformulating this phenomenological approach in terms of a Landau free energy expansion, we are dealing with coupled-order parameters, where $f\prime(T)$ corresponds to the Lifshitz invariant strain component, while g_T represents the field one. In view of the simplicity of the model, the agreement between experiment and theory is amazingly good.

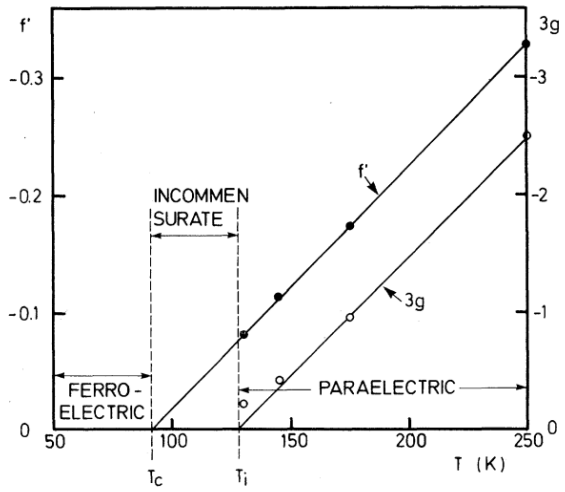

Figure 4. Temperature dependence of the coupling parameters g_T and $f\prime(T)$ in the paraelectric and incommensurate regimes.

4. Breather Solutions and Relaxor Ferroelectrics

For many years, it has been well known that perovskite oxides exhibit an enormous variety of ground states, induced by oxygen-doping or deficiencies and/or by the replace-

ments of the B or A sites by isovalent ions. The doped and mixed compounds are a platform for applications and new technologies. For these reasons, increased scientific research has focussed on their local and global properties, often employing novel tools. Especially, it has been shown that their average global and local structures vary considerably [41–46]. This implies that the Bloch theorem is no longer fulfilled, and conventional approaches can no longer be used. This intrinsic heterogeneity implies that large anharmonicity is inherent to these compounds, which suggests the formation of new intrinsic local modes (ILM) and discrete breather (DB)-bound states [47–50]. Generic solutions in the form of discrete breathers are time-periodic and (typically exponentially) localized in space. Discrete breathers are not confined to certain lattice dimensions. Necessary ingredients for their occurrence are the existence of upper bounds on the phonon spectrum (of small fluctuations around the ground state) of the system as well as the nonlinearity in the differential equations. The fascinating properties of these nonlinear solutions are that they are sources of energy localization and transport in nonlinear media.

A fundamental problem related to ILM and DB states is confining them to an energetically allowed stability regime, namely the gap region between the lowest optic and acoustic phonon modes. If the nonlinear modes lie above this gap, they are unstable and decay into the optic mode. In addition, it has been argued that hard-core nonlinearity is not realizable physically [49], where hard-core refers to negative values for the harmonic interaction, namely g_2, whereas the anharmonic one, g_4, is positive. The latter statement stems from the fact that a rigid ion or rigid spin-lattice potential has been considered for the calculations. Here, we instead use the polarizability model as defined by Equation (1), where charge transfer, dynamical covalency and hybridization effects are explicitly included.

Instead of the above discussed periodon solutions, the possible formation of DB is investigated [51], which requires that its frequency is constant within a limited spatial region and zero beyond that, which corresponds to a multi-vibrational quanta-bound state. In order to obtain the equations of motion, the displacement coordinates are assumed to be time-periodic:

$$u_{1n}(t) = A\xi_{1n}\cos(\omega t) \tag{7a}$$

$$u_{2n}(t) = B\xi_{2n}\cos(\omega t) \tag{7b}$$

$$w_{1n}(t) = C\eta_{1n}\cos(\omega t) \tag{7c}$$

with A, B, and C being the amplitudes and ξ, η the corresponding displacements. The amplitudes are obtained through the equations of motion and are frequency-dependent, and the electronic shells are treated in the adiabatic limit. The equations of motion are given by:

$$-m_1\omega^2\xi_{1n}A\cos(\omega t) = f'AD\xi_{1n}\cos(\omega t) + g_2C\eta_{1n}\cos(\omega t) + g_rC^{r-1}\eta_{1n}^{r-1}[\cos(\omega t)]^{r-1} \tag{8a}$$

$$-m_2\omega^2\xi_{2n}B\cos(\omega t) = fC(\eta_{1n+1} + \eta_{1n})\cos(\omega t) + fA(\xi_{1n+1} + \xi_{1n})\cos(\omega t) - 2fB\xi_{2n}\cos(\omega t) \tag{8b}$$

$$0 = -g_2C\eta_{1n} - g_rC^{r-1}\eta_{1n}^{r-1}[\cos(\omega t)]^{r-1} - 2fC\eta_{1n}\cos(\omega t) - 2fA\xi_{1n}\cos(\omega t) + fB(\xi_{2n-1} + \xi_{2n})\cos(\omega t) \tag{8c}$$

Here, r is the degree of anharmonicity. In order to reduce the number of degrees of freedom, Equation (8b) is replaced by one lattice constant:

$$-m_2\omega^2\xi_{2n-1}B\cos(\omega t) = fC(\eta_{1n-1} + \eta_{1n})\cos(\omega t) + fA(\xi_{1n-1} + \xi_{1n})\cos(\omega t) - 2fB\xi_{2n-1}\cos(\omega t) \tag{9}$$

Adding Equations (8b) and (9) and twice the adiabatic approximation yields:

$$\begin{aligned}(m_2\omega^2 - 2f)\left\{g_2C\eta_{1n}\cos(\omega t) + g_rC^{r-1}\eta_{1n}^{r-1}[\cos(\omega t)]^{r-1}\right\} + (m_2\omega^2 - 2f)[C\eta_{1n} + A\xi_{1n}]\cos(\omega t) = \\ -f^2\cos(\omega t)[CD\eta_{1n} + AD\xi_{1n}]\end{aligned} \tag{10}$$

Equations (10) and (8a) have analytical solutions that can be evaluated by the rotating wave approximation, namely:

$$\cos^p(\Theta) = \frac{p!}{2^{p-1}} \sum_{k=1}^{p} \frac{\cos(k\Theta)}{\left[\frac{p+k}{2}\right]!\left[\frac{p-k}{2}\right]!} \qquad p,k \equiv odd \tag{11}$$

$$\cos^{r-1}(\omega t) = C_r \cos(\omega t) + higher\ harmonics \tag{12}$$

with $C_r = \frac{(r-1)!}{2^{r-2}\left(\frac{r}{2}\right)!\left(\frac{r}{2}-1\right)!}$, where only the first term in the expansion is taken into account since all higher-order terms rapidly decrease. The so-called worst case, $r = 4$, is considered for systems with inversion symmetry, which excludes the case $r = 3$ and defines $C_r = 3/4$. The resulting potential is a hard-core nonlinear one if $g_2 < 0$, $g_4 > 0$ and a soft one if $g_2 > 0$, $g_4 > 0$. With the harmonic coupling being attractive and the anharmonic coupling repulsive, hard-core anharmonicity is given, which might turn into a soft one when lattice and ILM solutions are superimposed.

The equations of motion are thus similar to those obtained from Equation (1). Interesting novel solutions are obtained by the ansatz $w = -2u$, which yields complex results not discussed here. A rather natural choice for ILM's odd parity displacement patterns have been chosen, where at site $n = 0$, a dipole moment with "length" n_c is formed, which is compensated by the surrounding ordered lattice by creating at site n, counted from n_c, a dipole moment in the opposite direction with displacement ξ_n according to $\xi_n = \xi_0 - \frac{n}{2} : n \equiv even$; $\xi_n = -\left[\xi_0 - \frac{n}{2}\right] : n \equiv odd$. This choice guarantees that at lattice site n_c, the breather extensions have reached their limit. The spread of the breather spatial extensions depends on the magnitude of the central dipole moment. With the choice $\eta_n = -2\xi_n$, two solutions for ω are obtained, which need to be the same over all sites of the breather extent until n_c is reached (Figure 5 topleft). Figure 5 right provides an approximate description of the top figure in terms of a damped oscillator.

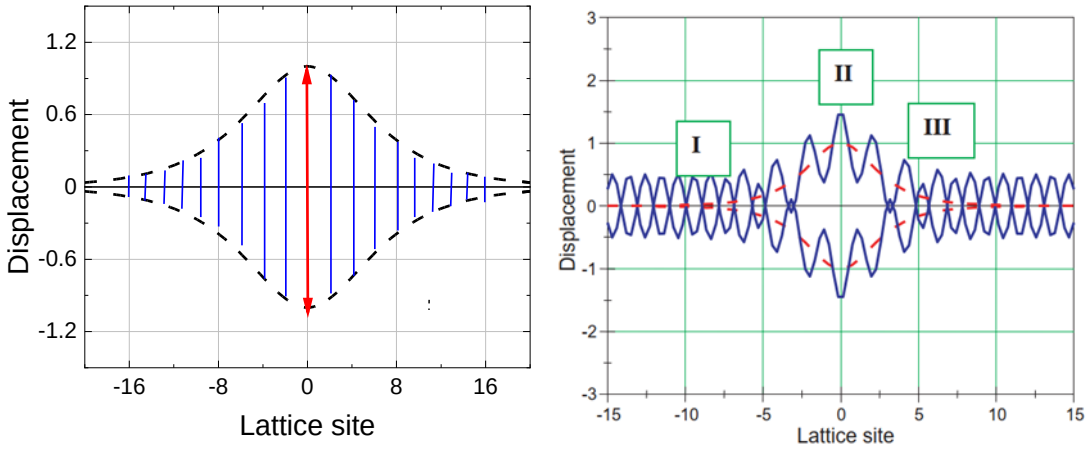

Figure 5. (**Left**) Displacements of ion 1 with mass m_1 within the breather region. The breather centre is marked by the red arrow. For clarity, ion 2 is omitted. The black line corresponds to an envelope function proportional to $1/\cosh$ and $-1/\cosh$. (**Right**) The displacement pattern stemming from the superposition of DB and regular lattice modes. I refers to the regular lattice modes, III defines a charge transfer region, and II corresponds to the DB centre. Region III is characterized by the mixing of DB and regular lattice displacement.

Thus, the breather spatial spread is $2n_c$ with small deviations for the n = 0 solution when g_4 becomes site-dependent, e.g., $\tilde{g}_4^{(n)} = g_4/2(n - n_c)^2$. The result is consistent with the fact that the double-well potential is steep and broad in the breather centre and becomes smoother with increasing n to be pseudo-harmonic for distances further apart. Simultaneously, this implies that the centre the electron is far apart from its core, delocalized

and spread over the whole DB extent, whereas at the boundaries, it is completely localized. This scenario closely resembles polaron physics, with the distinction that the electron is not trapped by the lattice distortion but moves almost freely through the distorted region.

The frequencies for the displacement patterns are given by:

$$\omega_1^2 = \frac{1}{m_1}\left[4f' + g\frac{C}{A}\right] - \frac{2f\prime}{n_c m_1} \tag{13a}$$

$$\omega_2^2 = \frac{2f}{m_2}[1 - \frac{1}{n_c}\frac{1}{2 + \frac{gC}{2f(2C-A)}}] \tag{13b}$$

with $g = 2g_2 + C_r\widetilde{g}_4C^2$. Outside the DB region, the frequencies are $\omega_1^2 = \frac{1}{m_1}\left(4f' + g\frac{C}{A}\right)$ and $\omega_2^2 = \frac{2f}{m_2}$. The existence regimes of the solutions Equation (13) are defined by comparing those to the SPA solutions. As already outlined above, these need to lie in the gap region between optic and acoustic modes, which excludes ω_2^2 from further considerations. However, ω_1^2 is also subject to certain restrictions, since this lies only in the gap regions if the following inequality is true: $(2\widetilde{f})^{1/2} < (g\frac{C}{A})^{1/2} < \left[\frac{2\widetilde{f}(m_1+m_2)}{m_2} - 4f'\right]^{1/2}$ This is correct. Apparently, a decisive role for the DB formation is played by the ionic masses, elasticity related to f', and the lattice stability, as determined by $2\widetilde{f} = 2fg_T/(2f + g_T)$. Elastic softness clearly supports DB formation, whereas lattice stability does not contribute significantly.

Analogous to the periodon solutions, the interplay between the lattice and DB modes can be explored by a linear superposition of the corresponding displacement patterns. This leads to a stabilization of the phonon frequencies, where even in the case of $g_T = 0$, the coupling to the breather prevents a freezing of any soft mode. This enlarges the DB existence regime. Conversely, the breather adopts a temperature dependence, since g_2 is replaced by g_T, which renormalizes its potential from hard-core to soft. This ansatz has the consequence that the dynamical interplay between the regular lattice and the locally distorted regions manifests as strongly enhanced diffuse scattering, e.g., as observed in relaxor ferroelectrics. Especially, ghost modes may be observed, which take away spectral weight from the regular lattice modes at certain wave vectors, as defined by the DB spatial extent. Three regions of the coupled modes can be differentiated (Figure 5 right): I, the regular lattice modes; III, a charge-transfer regime where the lattice mode amplitude is modified by the breather; and II, where the breather centre induces large distortions with almost freely moving charges. Since the nonlinearity, as defined by g_4, becomes site-dependent, the dielectric response ε also varies locally. This is what is observed in relaxor ferroelectrics, where ε is frequency-dependent and indicates that ILM formation could be the origin [52–55]. Of course, the modelling of relaxor ferroelectrics described above does not fully capture the consideration of structural disorder, random fields, and related heterogeneity, including dynamic and static polar nanoregions (PNRs) (for a comprehensive review, see, e.g., Ref. [56]); however, essential features such as the frequency dependence of the dielectric response, its temperature dependence, and local charge transfer are well described.

5. Domains and Domain Walls

An alternative approach was developed for when phonon anharmonicity is beyond perturbation theory and is transformed into solitary waves [57,58]. These excitations are often better understood in a quasi-static context where their dynamics are considered separately from their phonon origins. The probably most obvious example for such solitary waves is a twin boundary. As an example, when $SrTiO_3$ undergoes the symmetry-breaking phase transition near 105 K, the low-temperature phase is commonly riddled with twin domains [59–62]. These twin domains have been the bane of most research, and a common approach has been to simply ignore them. This is justifiable because the twist between twin domains is small, and each twin domain follows very closely the same physics of any other

twin domain or even of an entire, untwinned sample. These 'bulk' properties are hardly influenced by the twins, and twinning was considered a nuisance at best. This is not true for the geometrical joints between the twin domains, namely the twin boundaries (or twin walls). Since 2010, research on twin walls has massively expanded because it was discovered that these twin walls house many new and useful physical properties that the bulk do not possess. These 'emerging' properties include polarity, (ionic and super) conductivity, photovoltaic effect, and pn junctions [63–68]. There is another dynamic wall property that is widely used. Most twin walls are mobile under external forcing when pinning is weak [68–72]. This means that small external stresses, such as the tip of a preparation needle, will move domain walls to desired positions. Even without external forces, domain walls can be moved by thermal stresses depending on the shape of the sample [73–79]. Importantly, twin walls often interact. They also contain internal geometrical structures, namely kinks, which represent walls in walls and lead to additional excitations where such kinks move at supersonic speed [77]. We now focus on the dynamical features in the 'critical slowing down' regime in both phases and relate them to the interactions and correlations [58,70] between interfaces such as twin walls. The movement of correlated twin walls, with and without external forcing, often occurs in avalanches. Such avalanches are known to geophysicists from earthquakes. Avalanches in nano-materials have come to the forefront and dominate much of the current research [80,81]. Their experimental incarnation is often called 'crackling noise' [82].

The concept of crackling noise has been around for a long time. It refers to the jerky response of many systems to a slowly changing driving force or field. For example, a piece of paper crackles when it is slowly crumpled, and corn flakes crackle when you pour milk over them. Breaking a chopstick [83] or a piece of coal or sandstone leads to audible crackles [84] and can easily be measured by putting microphones next to the sample [85]. Other examples include the braking of bones [86] or the destruction of kidney stones in operating theatres [87]. Earthquakes follow similar patterns [88–90]. Similarly, magnetic materials magnetize via jumps in the magnetization that span a wide range of jump sizes. These jumps were originally observed as crackling Barkhausen noise when a search coil was wrapped about the sample and hooked up to a loudspeaker [91,92]. Starting with the Barkhausen analysis of magnetization jumps in slowly magnetized ferromagnetics, the concept of crackles with a broad (power-law) size distribution was generalized to crackling noise because it was found that similar phenomena are surprisingly widespread [80,82,93].

Anharmonic phonons transmute hence to domain walls that have, like phonons, some universal properties. Renormalization group calculations suggest that, on long-length scales, the avalanche systems of domain walls flow to the same fixed point under coarse graining, which suggests that their scaling behaviour is the same for all systems [94,95]. Important open questions concern the size of the underlying universality class, i.e., how many systems show the same crackling noise statistics. This is often quantified by power laws and scaling functions underlying the avalanche size and duration distributions, the power spectra of acoustic emissions (AEs), and related quantities. The power law distributions of crackling noise also imply that these processes are scale-invariant: each measurement interval shows exactly the same functional form of the jerk probability. This scale invariance is absolutely stunning because, in many large systems, it extends over 8 decades of the crackling noise energy and is truncated only by the limitations of the electronic equipment that measures the different jerk parameters [e.g., 80]. It is rare to find physical laws in solid-state physics that have excellent validity over 8 energy decades! A large body of experimental studies have proven these ideas to be largely correct. The power laws of the various observables are very similar indeed, including the energy, amplitude and size exponents, and the duration of the excitation. The universality of the crackling noise is further focused because energy exponents in ferroic materials are often near the mean field (MF) values of 1.33 and 1.66, while higher values were measured more rarely in other systems [80].

In this chapter, we propose that domain boundaries evolve out of anharmonic phonons. This gives the system an order–disorder component that coexists with the phonon degrees of freedom. Alternatively, starting from an order–disorder spin model, Salje and Dahmen [80] have argued that very simple theoretical models can describe domain wall avalanches rather well. Using magnets as an instructive case, the random-field Ising model (RFIM), with or without added long-range dipolar interactions, is a typical example. In the RFIM, the material is modelled as a cubic crystal with N sites, each with a spin S_i = +−Yes, it should be plus/minus1, i = 1... N. The Hamiltonian for the RFIM is $H = -\sum_{ij} J_{ij} S_i S_j - (H_{ext}(t) + h_i) S_i$, where the first term represents the ferromagnetically coupled nearest neighbours (with nearest-neighbour coupling $J_{ij}[J < 0]$), $H_{ext}(t)$ is the external applied field, and h_i is the quenched local random magnetic field with Gaussian distribution. In the simplest non-equilibrium dynamics, each spin is aligned with its local effective field, $h_{j,\,effective} = -\sum_{ij} J_{ij} S_i S_j + H_{ext}(t) + h_i)$. As the external magnetic field is slow compared to h_i, it triggers spins with positive random fields to flip from down ($S_j = -1$) to up ($S_j = +1$) whenever their local effective field first becomes positive. Because of the ferromagnetic coupling between the spins, each such spin flip can trigger neighbouring spins to also flip, causing a spin-flip avalanche. In the adiabatic limit, the external driving field is kept fixed until an avalanche is completed. Only afterward is it increased until the next spin flips. We call S the size of a spin-flip avalanche. Two limiting cases are illustrative for avalanches. In a pure system with all random fields, one expects that all spins will flip in one giant spin-flip avalanche that covers the entire system. For infinite disorder, the random fields are so far apart that each spin flips separately, and there are no large spin-flip avalanches. The model predicts that between these two extremes at a critical disorder, a power-law avalanche size distribution [D(S)] is observed when the magnetic field is near a critical field (H_c). The power law is multiplied with an exponential cut-off if H is tuned away from H_c or the disorder is tuned away from the critical disorder. The predictions only depend on general properties, such as symmetries, dimensions, range of interactions, etc. Many more quantities have been predicted, but the scaling form of the avalanche size distribution is quite general. This picture appears valid for ferroic domain walls and has been advocated for the behaviour of $SrTiO_3$ [96] and $BaTiO_3$ [81].

For soft magnets, the coupling J_{ij} is generalized to also include added long-range dipolar interactions, and simplified power laws apply. Twin walls follow the same non-equilibrium pathways with typical avalanche exponents near mean field values. Changing the RFIM to a 'soft' spin model with long-ranging elastic interactions leads then to the same coexistence between phonon and domain walls.

6. $SrTiO_3$ as an Example

$SrTiO_3$ undergoes a second-order phase transition with one transverse acoustic soft mode at high temperatures, which splits into two soft modes in the symmetry-broken phase. In addition, domain walls appear, and their characteristics are shown in Figure 6. Above the transition point, near 106.5 K, a large precursor regime is seen by elastic softening (Figure 6b). Below the transition point, domains form and increase the damping of the acoustic wave (Figure 6a). The domain walls freeze with a very small pinning energy and, on cooling, form clusters. These clusters give the crystal a glassy or solid damping behaviour with greatly diminished elastic Young modulus [96].

In $SrTiO_3$, as expected, even more complex jerky avalanches were observed [97]. The movement of the twin walls under weak external forcing is shown in Figure 6. Close to the transition point, the walls are so weakly pinned that their mutual interaction dominates, and the domain wall pattern fluctuates like in a liquid. In the pinned regime, jerks and avalanches are observed, and below 40 K, quantum effects destroy individual avalanches and lead to strongly coupled movements of clusters. The avalanches are seen as random jerks when the external strain exceeds some 10^{-7} and unpins the walls (Figure 6c).

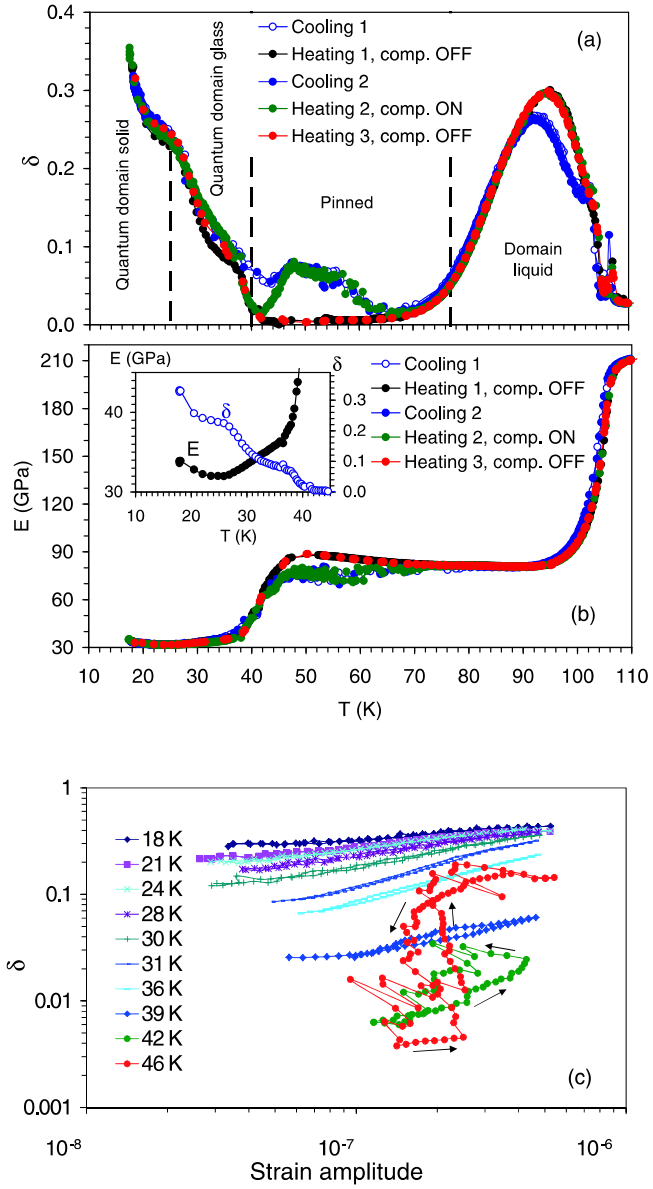

Figure 6. Domain wall characteristics in $SrTiO_3$ with (**a**) the damping of acoustic waves, (**b**) the elastic modulus, and (**c**) the damping as function of the applied strain. The strain amplitudes are extremely small and can be generated simply by heating or cooling samples with irregular shapes. Some unpinning already happens when the sample is cooled in a cryostat, with the noise of the cryostat as the sole unpinning force. Measurements were made under 'silent' conditions [97].

We now discuss the interaction between twin walls, which is crucial for avalanche formation [98]. The observed glassy behaviour [97] and the very existence of avalanches require such interactions, which appears counterintuitive following the work of Lajzerowicz and Levanyuk [99]. They and others showed that such interactions are extremely weak unless domain walls intersect [100]. While this argument is correct, we need to consider a further dimensional reduction. While domain walls are planes with some 1 nm thickness, they host walls inside these wall [62]. These finer walls are often geometrical kinks that emit strong strain fields. These kink–kink strain fields interact like monopoles (~1/r where r is the distance between kinks) if the twin wall is inside the bulk and like dipoles (~$1/r^2$) close to surfaces. This weakening of interactions is due to elastic image forces and has been shown experimentally by investigations of thin, freestanding sample lamellae [73,77,78,100]. The long-ranging strain interaction between kinks leads to effective wall–wall interactions like spin–spin interactions in spin glasses [101].

7. Precursor Effects in $SrTiO_3$

Anharmonic phonons become solitary waves and ultimately contribute to domain walls. Domain walls occur in the symmetry-broken phase, but very similar excitations are seen also in high-temperature phases. At temperatures above the transition point, we find precursor clusters that have properties very similar to those of wall-dominated systems in the symmetry-broken phase. Experimentally, the measurement of the temperature evolution of the elastic moduli was very successful in demonstrating this precursor effect [102]. In a simple soft-mode model, the moduli transform stepwise in improper ferroelastics [103,104] with no temperature evolution at $T > T_c$. This behaviour is hardly ever observed, and typical lowering or enhancement of the moduli when approaching T_c in a second-order phase transition is commonly observed. The scaling of the elastic moduli follows a power law $E \sim E_0 \, |T - T_c|^{-\kappa}$, where κ is the precursor exponent. These exponents depend on the dispersion of the soft modes and hence on the dimensionality of the softening in reciprocal space. In a very simple model, values of κ have been predicted to be 1.5 if a single phonon branch flattens. If two orthogonal phonon branches flatten while the third remains relatively steep, we expect $\kappa = 1$. Finally, if three orthogonal branches flatten, the expected value is $\kappa = 0.5$. The experimental observations are surprisingly close to these values in $SrTiO_3$. The range of exponents is typically between 0.5 and 2 in most domain wall systems. The power-law dependence is well demonstrated, with an exponent $\kappa \sim 0.2$ for $BaTiO_3$ and 1.8 for $SrTiO_3$ [102]. Alternative Vogel–Fulcher fits

$$\Delta C_{ik} = B_{ik} exp\left(\frac{E_a/k_B}{T - T_{VF}}\right) \tag{14}$$

are also shown in Figure 7. Here, the activation energy is E_a, and the Vogel–Fulcher temperature is T_{VF}. Typically, distinguishing between power laws and Vogel–Fulcher statistics is extremely difficult. In $SrTiO_3$, Cordero et al. and Ishibashi and Iwata [102,103] have argued that the power law gives a better agreement with the experimental data. The precursor regime extends in $SrTiO_3$ to 125 K; other materials show similar or larger is okprecursor temperature intervals (e.g., [105]).

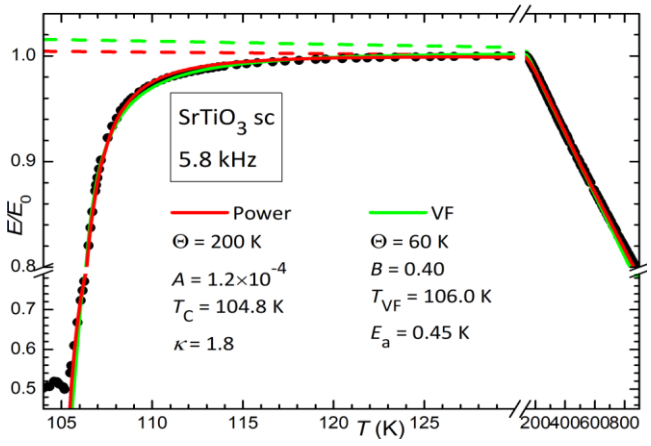

Figure 7. Elastic precursor softening in $SrTiO_3$. The red and green lines represent the power law and the Vogel–Fulcher fits, respectively; the dotted lines are the baseline for the moduli at higher temperatures (after [102]).

The softening of the elastic moduli is not purely a phonon effect. In a very simple model of an anharmonic Landau system [100], the crystalline structure inside the precursor regime was investigated by molecular dynamics simulations. The anharmonicity is a sheared NaCl-type structure that was simulated by anharmonic springs in the ball and strings model in Figure 8.

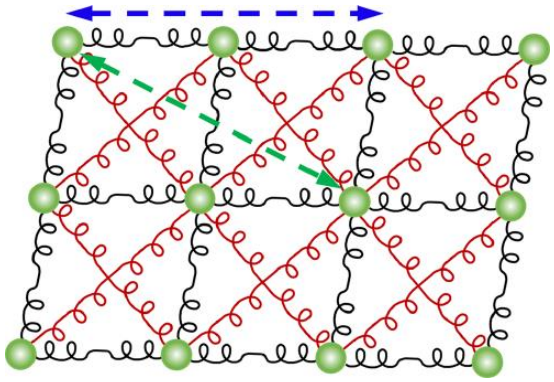

Figure 8. Ball and spring model for phonons and domain walls. The red springs are Landau springs with two energy minima.

The potentials are

$$Black\ springs U(r) = 0.1\Big(r-1\Big)^2 \tag{15a}$$

$$Red\ springs U(r) = -0.05(r-2)^2 + 40(r-2)^4 \tag{15b}$$

along diagonals in the lattice unit, which has two energy minima and generates the Landau potential. The fourth-order third-nearest interactions are given as:ok

$$U(r) = 0.04(r-2)4 \text{ (blue arrow)}, \tag{15c}$$

and an anharmonic fourth-nearest Landau-type double-well interaction is given as:ok

$$U\ (r) = -0.05(r-\sqrt{5})^2 + 25.5(r-5)^4 \text{ (green arrow)}, \tag{15d}$$

Models of this kind have been successfully used to investigate ferroelastic materials [106] and phase transitions and to reproduce both phonons and nano-structures very well [107]. They show the correct softening as measured in $SrTiO_3$ and show the related nano-structure in Figure 9.

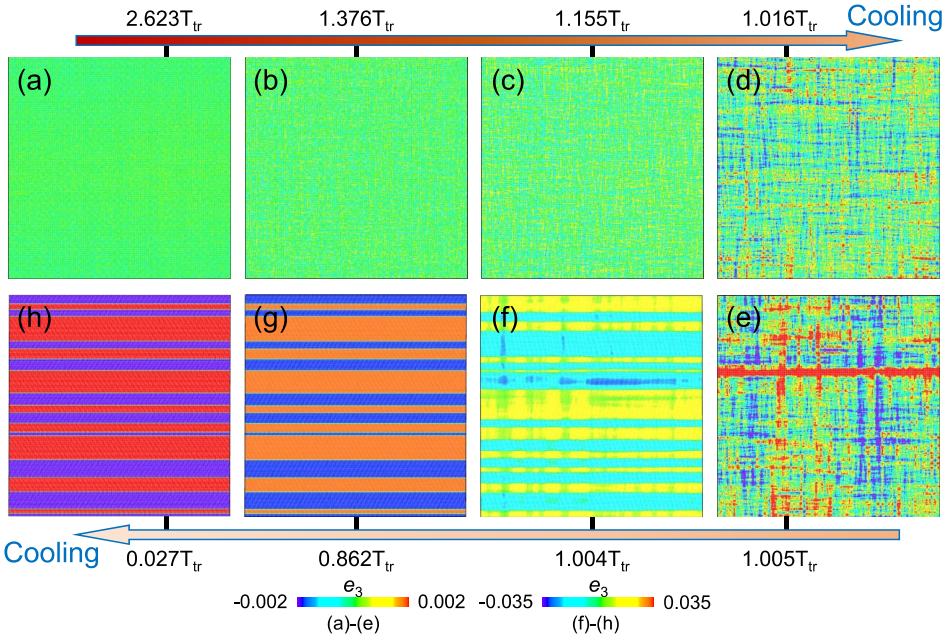

Figure 9. Nano-structures that spontaneously nucleate with the model in Figure 8. T_{tr} is the transition temperature T_c in $SrTiO_3$. In the symmetry-broken phase, twin walls are clearly visible (**f**–**h**). At higher

temperatures the system is homogeneous (**a**), with lowering the temperature wall-like nano-structures appear at (**b**,**c**) and become dominant in (**d**). These precursor structures reduce the relevant elastic modulus and link the anharmonic phonons at high temperatures with the domain walls at low temperatures [104].

This remarkable result shows that fine structures are visible at temperatures as high as 1.4 T_c and become very strong at 1.016 T_c, while the time-averaged structure is firmly in the high-temperature phase. The structural deformation resembles the typical tweed structure in order/disorder phase transitions [108–114], with a closely interwoven domain pattern. The domain structures seem to emerge in these structures, although they are dynamic excitations that fluctuate and eliminate the actual symmetry-breaking of the phase transition. Such excitations can be described as highly anharmonic 'phonon' branches or as solitary waves. When the actual phase transition occurs, stable domain walls appear (f–h), which are no longer described by phonon excitations.

8. Summary and Conclusions

In summary, we have shown that the central peak and 'critical slowing down' regimes are characterised by the appearance of mobile, short-lived domain wall excitations that emerge out of phonon branches at higher temperatures. This idea refines the interpretation by Alex Müller, where terms like 'entropic clusters' were used to describe what is rather like the features summarized in this paper. The emerging mechanism can then be depicted as follows: at $T >> T_c$, phonons are harmonic and become weakly anharmonic under cooling when the soft mode lowers the frequency. Above but near T_c, the phonon amplitudes increase, and the frequencies collapse. This leads to highly anharmonic phonons that can be described by higher-order dispersion terms like in periodons, as observed in the rather complex K_2SeO_4 compound, but also in simple binary ferroelectrics as, e.g., SnTe. Structurally, local clusters appear already at 1.4 T_c in our simulations. They are widely separated. They grow and form denser patterns when approaching T_c. Characteristic temperatures have been defined to describe this process. While the lifetime of these clusters is much longer than the phonon time, they remain dynamic. At the transition point, the clusters form domains with long-lived domain boundaries that still contain features of the precursor clusters. Lowering the temperature even further can lead (e.g., in $SrTiO_3$) to strong interactions between domains, domain walls and kinks inside domain walls, and to the formation of quantum domain glasses and quantum domain solids. Specifically, we have addressed the interconnection between phonons, domain walls and nonlinear excitations, which are common to the lattice as well as to domains and form a link between them.

Author Contributions: Conceptualization and writing are equally distributed under E.K.H.S. and A.B.-H. All authors have read and agreed to the published version of the manuscript.

Funding: EKHS is grateful to EPSRC (Grant EP/P024904/1).

Data Availability Statement: All data are available upon request to the suthors.

Conflicts of Interest: The authors declare no conflict of interests.

References

1. Landau, L.D. On the theory of phase transitions. *Phys. Z. Sowjetunion* **1937**, *11*, 19–32. [CrossRef]
2. Landau, L.D.; Lifshitz Evgeny, M. *Statistical Physics*, 3rd ed.; Butterworth-Heinemann: Oxford, UK, 1980; Volume 5, ISBN 978-0-7506-3372-7.
3. Cochran, W. Crystal Stability and the Theory of Ferroelectricity. *Phys. Rev. Lett.* **1959**, *3*, 412–415. [CrossRef]
4. Müller, K.A.; Berlinger, W. Behavior of $SrTiO_3$ near the [100]-stress-temperature bicritical point. *Phys. Rev. Lett.* **1975**, *35*, 1547–1550. [CrossRef]
5. Müller, K.A.; Berlinger, W. Static critical exponents at structural phase transitions. *Phys. Rev. Lett.* **1971**, *26*, 13–17. [CrossRef]
6. Aharony, A.; Bruce, A.D. Polycritical points and flop-like displacive transitions in Perovskites. *Phys. Rev. Lett.* **1974**, *33*, 427–430. [CrossRef]

7. O'Ariano, G.; Aldrovandi, S.; Rigamonti, A. Critical behavior of the order parameter at antiferrodistortive transitions with cubic fluctuations. *Phys. Rev. B* **1982**, *25*, 7044. [CrossRef]
8. Bellaiche, L.; Íñiguez, J. Universal collaborative couplings between oxygen-octahedral rotations and antiferroelectric distortions in perovskites. *Phys. Rev. B* **2013**, *88*, 014104. [CrossRef]
9. Cochran, W. Crystal Stability and the Theory of Ferroelectricity. *Adv. Phys.* **1960**, *9*, 387–423. [CrossRef]
10. Thomas, H. *Structural Phase Transitions and Soft Modes*; Samuelsen, E.J., Andersen, E.J., Feder, J., Eds.; Universitetsforlaget: Oslo, Norway, 1971; p. 15.
11. Salje, E.K.H.; Wruck, B.; Thomas, H. Order-parameter saturation and low-temperature extension of Landau theory. *Z. Phys. B* **1991**, *82*, 399–404. [CrossRef]
12. Lines, M.E.; Glass, A.M. *Principles and Applications of Ferroelectrics and Related Materials*; Clarendon Press: Oxford, UK, 1977; 52p.
13. Gryaznov, D.; Blokhin, E.; Sorokine, A.; Kotomin, E.A.; Evarestov, R.A.; Bussmann-Holder, A.; Maier, J. A Comparative Ab Initio Thermodynamic Study of Oxygen Vacancies in ZnO and $SrTiO_3$: Emphasis on Phonon Contribution. *J. Phys. Chem. C* **2013**, *117*, 13776–13784. [CrossRef]
14. Müller, K.A.; Burkard, H. $SrTiO_3$: An intrinsic quantum paraelectric below 4 K. *Phys. Rev. B* **1979**, *19*, 3593–3602. [CrossRef]
15. Migoni, R.; Bilz, H.; Bäuerle, D. Origin of Raman Scattering and Ferroelectricity in Oxidic Perovskites. *Phys. Rev. Lett.* **1976**, *37*, 1155–1158. [CrossRef]
16. Bilz, H.; Benedek, G.; Bussmann-Holder, A. Theory of ferroelectricity: The polarizability model, Phys. *Rev. B* **1987**, *35*, 4840–4848. [CrossRef]
17. Bussmann-Holder, A. The polarizability model for ferroelectricity in perovskite oxides. *J. Phys. Condens. Matter.* **2012**, *24*, 273202. [CrossRef]
18. Ko, J.-H.; Górny, M.; Majchrowski, A.; Roleder, K.; Bussmann-Holder, A. Mode softening, precursor phenomena, and intermediate phases in $PbZrO_3$. Phys. *Rev. B* **2013**, *87*, 184110. [CrossRef]
19. Bussmann-Holder, A.; Roleder, K.; Ko, J. What makes the difference in perovskite titanates? *J. Phys. Chem. Solids* **2018**, *117*, 148–157. [CrossRef]
20. Bussmann-Holder, A.; Keller, H.; Simon, A.; Bihlmayer, G.; Roleder, K.; Szot, K. Unconventional Co-Existence of Insulating Nano-Regions and Conducting Filaments in Reduced $SrTiO_3$: Mode Softening, Local Piezoelectricity, and Metallicity. *Crystals* **2020**, *10*, 437. [CrossRef]
21. Burns, G.; Dacol, F. Crystalline ferroelectrics with glassy polarization behaviour. *Phys. Rev. B* **1983**, *28*, 2527–2530. [CrossRef]
22. Wang, C.L.; Zhao, M.L. Burns temperature and quantum temperature scale. *J. Adv. Dielectr.* **2011**, *1*, 163–167. [CrossRef]
23. Bussmann-Holder, A.; Beige, H.; Völkel, G. Precursor effects, broken local symmetry, and coexistence of order-disorder and displacive dynamics in perovskite ferroelectrics. *Phys. Rev. B* **2009**, *79*, 184111. [CrossRef]
24. Stachiotti, M.; Dobry, A.; Migoni, R.; Bussmann-Holder, A. Crossover from a displacive to an order-disorder transition in the nonlinear-polarizability model. *Phys. Rev. B* **1993**, *47*, 2473–2479. [CrossRef] [PubMed]
25. Ko, J.-H.; Roleder, K.; Bussmann-Holder, A. Instabilities in the ferro- and antiferroelectric lead perovskites driven by transition metal ion mass: From $PbTiO_3$ via $PbZrO_3$ to $PbHfO_3$. *J. Phys. Cond. Mat.* **2014**, *26*, 275402.
26. Simoes, Z.; Riccardi, C.S. Dielectric Spectroscopy Analyses of $SrBi_4Ti_4O_{15}$ Films Obtained from Soft Chemical Solution. *Adv. Mat. Sci. Eng.* **2009**, *2009*, 928545. [CrossRef]
27. Zhang, N.; Yokota, H.; Glazer, A.M.; Thomas, P.A. The not so simple cubic structure of $PbZr_{1-x}Ti_xO_3$ (PZT): Complex local structural effects in perovskites. *Acta Cryst. B* **2011**, *67*, 461–466. [CrossRef]
28. Carpenter, M.A. Static and dynamic strain coupling behaviour of ferroic and multiferroic perovskites from resonant ultrasound spectroscopy. *J. Phys. Condens. Matter* **2015**, *27*, 263201. [CrossRef] [PubMed]
29. Piskunov, S.; Heifets, E.; Eglitis, R.I.; Borstel, G. Bulk properties and electronic structure of $SrTiO_3$, $BaTiO_3$, $PbTiO_3$ perovskites: An ab initio HF/DFT study. *Comput. Mater. Sci.* **2004**, *29*, 165–178. [CrossRef]
30. Salje, E.K.H.; Carpenter, M.A.; Nataf, G.F.; Picht, G.; Webber, K.; Weerasinghe, J.; Lisenkov, S.; Bellaiche, L. Elastic excitations in $BaTiO_3$ single crystals and ceramics: Mobile domain boundaries and polar nanoregions observed by resonant ultrasonic spectroscopy. *Phys. Rev. B* **2013**, *87*, 014106. [CrossRef]
31. Ko, J.-H.; Kim, T.H.; Roleder, K.; Rytz, D.; Kojima, S. Determination of elastic stiffness coefficients of lead zirconate single crystals in the cubic phase by Brillouin light scattering. *Phys. Rev. B* **2011**, *84*, 094123. [CrossRef]
32. Völkel, G.; Müller, K.A. Order-disorder phenomena in the low-temperature phase of $BaTiO_3$. *Phys. Rev. B* **2007**, *76*, 094105. [CrossRef]
33. Bussmann, A.; Bilz, H.; Roenspiess, R.; Schwarz, K. Oxygen polarizability in ferroelectric phase transitions. *Ferroelectrics* **1980**, *25*, 343–346. [CrossRef]
34. Tessman, G.R.; Kahn, A.H.; Shockley, W. Electronic Polarizabilities of Ions in Crystals. *Phys. Rev.* **1953**, *92*, 890. [CrossRef]
35. Bishop, A.R.; Krumhansl, J.A.; Trullinger, S.E. Solitons in condensed matter: A paradigm. *Physica* **1980**, *1*, 1–44. [CrossRef]
36. Bilz, H.; Büttner, H.; Bussmann-Holder, A.; Kress, W.; Schröder, U. Nonlinear Lattice Dynamics of Crystals with Structural Phase Transitions. *Phys. Rev. Lett.* **1982**, *48*, 264–267. [CrossRef]
37. Pawley, G.S.; Cochran, W.; Cowley, R.A.; Dolling, G. Diatomic Ferroelectrics. *Phys. Rev. Lett.* **1966**, *17*, 753–756. [CrossRef]
38. Cowley, E.R.; Darby, J.K.; Pawley, G.S. The lattice dynamics of tin telluride. *J. Phys. C* **1969**, *2*, 1916. [CrossRef]
39. Iizumi, M.; Axe, J.D.; Shirane, G.; Shimaoka, K. Structural phase transformation in K_2SeO_4. *Phys. Rev. B* **1977**, *15*, 4392. [CrossRef]

40. Yamada, N.; Ikeda, T. Incommensurately modulated structure of K_2SeO_4. *J. Phys. Soc. Jpn.* **1984**, *53*, 2555–2564. [CrossRef]
41. Fäth, M.; Freisen, S.; Menovsky, A.A.; Tonioka, Y.; Aarts, J.; Mydosh, J.A. Spatially Inhomogeneous Metal-Insulator Transition in Doped Manganites. *Science* **1999**, *285*, 1540–1542. [CrossRef]
42. Pan, S.H.; Hudson, E.W.; Lang, K.M.; Eisaki, H.; Uchida, S.; Davis, J.C. Microscopic electronic inhomogeneity in the high-T_c superconductor $Bi_2Sr_2CaCu_2O_{8+x}$. *Nature* **2001**, *413*, 282–285. [CrossRef]
43. Pan, S.H.; Hudson, E.W.; Lang, K.M.; Eisaki, H.; Uchida, S.; Davis, J.C. Imaging the effects of individual zinc impurity atoms on superconductivity in $Bi_2Sr_2CaCu_2O_{8+\delta}$. *Nature* **2000**, *403*, 746–750. [CrossRef]
44. Saini, N.L.; Lanzara, A.; Bianconi, A.; Oyanagi, H. Local structural features of the superconducting $Bi_2Sr_2CaCu_2O_{8+\delta}$ system: A polarized Cu K-edge XAS study. *Phys. Rev. B* **1998**, *58*, 11768–11773. [CrossRef]
45. Islam, Z.; Liu, X.; Sinha, S.K.; Lang, J.C.; Moss, S.C.; Haskel, D.; Srajer, G.; Wochner, P.; Lee, D.R.; Haeffner, F.D.; et al. Four-unit-cell superstructure in the optimally doped $YBa_2Cu_3O_{6.92}$ superconductor. *Phys. Rev. Lett.* **2004**, *93*, 157008.
46. Li, F.; Zhang, S.; Damjanovic, D.; Chen, L.-Q.; Shrout, T.R. Local Structural Heterogeneity and Electromechanical Responses of Ferroelectrics: Learning from Relaxor Ferroelectrics. *Adv. Funct. Mater.* **2018**, *28*, 1801504. [CrossRef]
47. Sato, M.; Hubbard, B.E.; Sievers, A.J.; Ilic, B.; Czaplewski, D.A.; Craighead, H.G. Observation of Locked Intrinsic Localized Vibrational Modes in a Micromechanical Oscillator Array. *Phys. Rev. Lett.* **2003**, *90*, 044102. [CrossRef] [PubMed]
48. Vulgarakis, N.K.; Kalosakas, G.; Bishop, A.R.; Tsironis, G.P. Multiquanta breather model for PtCl. *Phys. Rev. B* **2001**, *64*, 020301. [CrossRef]
49. Kiselev, S.A.; Lai, R.; Sievers, A.J. Intrinsic resonant modes for a one-dimensional lattice with a soft optic mode. *Phys. Rev. B* **1998**, *57*, 3402–3405. [CrossRef]
50. Wang, W.Z.; Gammel, J.T.; Bishop, A.R.; Salkola, M.I. Quantum Breathers in a Nonlinear Lattice. *Phys. Rev. Lett.* **1996**, *76*, 3598–3601. [CrossRef]
51. Bussmann-Holder, A.; Bishop, A.R. Inhomogeneity, local mode formation, and the breakdown of the Bloch theorem in complex charge transfer systems as a consequence of discrete breather formation. *Phys. Rev. B* **2004**, *70*, 184303. [CrossRef]
52. Macutkevic, J.; Banys, J.; Bussmann-Holder, A.; Bishop, A.R. Origin of polar nanoregions in relaxor ferroelectrics: Nonlinearity, discrete breather formation, and charge transfer. *Phys. Rev. B* **2011**, *83*, 184301. [CrossRef]
53. Bussmann-Holder, A.; Bishop, A.R.; Egami, T. Relaxor ferroelectrics and intrinsic inhomogeneity. *Europhys. Lett.* **2005**, *71*, 249–255. [CrossRef]
54. Johansson, M.; Aubry, S. Growth and decay of discrete nonlinear Schrödinger breathers interacting with internal modes or standing-wave phonons. *Phys. Rev. E* **2000**, *61*, 5864. [CrossRef] [PubMed]
55. Zhao, X.-G.; Wang, Z.; Malyi, O.I.; Zunger, A. Effect of static local distortions vs. dynamic motions on the stability and band gaps of cubic oxide and halide perovskites. *Mater. Today* **2021**, *49*, 107–122. [CrossRef]
56. Kleemann, W. The relaxor enigma—Charge disorder and random fields in ferroelectrics. *Front. Ferroelectr. J. Mat. Sci.* **2006**, *1*, 29–136. [CrossRef]
57. Salje, E.K.H. Ferroelastic Materials. *Ann. Rev. Mater. Res.* **2012**, *42*, 265–283. [CrossRef]
58. Salje, E.K.H. Multiferroic Domain Boundaries as Active Memory Devices: Trajectories Towards Domain Boundary Engineering. *Chem. Phys. Chem.* **2010**, *11*, 940–950. [CrossRef]
59. Khomskii, D.I. Multiferroics: Different ways to combine magnetism and ferroelectricity. *J. Magn. Magn. Mater.* **2006**, *306*, 1–8. [CrossRef]
60. Nova, T.F.; Disa, A.S.; Fechner, M.; Cavalleri, A. Metastable ferroelectricity in optically strained $SrTiO_3$. *Science* **2019**, *364*, 1075–1079. [CrossRef]
61. Li, Y.L.; Choudhury, S.; Haeni, J.H.; Biegalski, M.D.; Vasudevarao, A.; Sharan, A.; Ma, H.Z.; Levy, J.; Gopalan, V.; Trolier-McKinstry, S.; et al. Phase transitions and domain structures in strained pseudocubic (100) $SrTiO_3$ thin films. *Phys. Rev. B* **2006**, *73*, 184112.
62. Salje, E.K.H.; Aktas, O.; Carpenter, M.A.; Laguta, V.V.; Scott, J.F. Domains within Domains and Walls within Walls: Evidence for Polar Domains in Cryogenic $SrTiO_3$. Phys. *Rev. Letters* **2013**, *111*, 247603. [CrossRef]
63. Van Aert, S.; Turner, S.; Delville, R.; Schryvers, D.; Van Tendeloo, G.; Salje, E.K.H. Direct Observation of Ferrielectricity at Ferroelastic Domain Boundaries in $CaTiO_3$ by Electron Microscopy. *Adv. Mater.* **2012**, *24*, 523–527. [CrossRef]
64. Aird, A.; Salje, E.K.H. Sheet superconductivity in twin walls: Experimental evidence of WO_{3-x}. *J. Phys. Cond. Mat.* **1998**, *10*, L377–L380. [CrossRef]
65. Seidel, J.; Maksymovych, P.; Batra, Y.; Katan, A.; Yang, S.Y.; He, Q.; Baddorf, A.P.; Kalinin, S.V.; Yang, C.H.; Yang, J.C.; et al. Domain Wall Conductivity in La-Doped $BiFeO_3$. *Phys. Rev. Lett.* **2010**, *105*, 197603.
66. Yang, S.Y.; Seidel, J.; Byrnes, S.J.; Shafer, P.; Yang, C.H.; Rossell, M.D.; Yu, P.; Chu, Y.H.; Scott, J.F.; Ager, J.W., III; et al. Above-bandgap voltages from ferroelectric photovoltaic devices. *Nat. Nanotechnol.* **2010**, *5*, 143–147. [CrossRef] [PubMed]
67. Paillard, C.; Bai, X.; Infante, I.C.; Guennou, M.; Geneste, G.; Alexe, M.; Kreisel, J.; Dkhil, B. Photovoltaics with Ferroelectrics: Current Status and Beyond. *Adv. Mater.* **2016**, *28*, 5153–5168.
68. Strikha, M.V.; Morozovska, A.N. Limits for the graphene on ferroelectric domain wall p-n-junction rectifier for different regimes of current. *J. Appl. Phys.* **2016**, *120*, 214101. [CrossRef]
69. Nguyen, C.P.T.; Schoenherr, P.; Salje, E.K.H.; Seidel, J. Crackling Noise Microscopy. *Nat. Commun.* **2023**, *14*, 4963. [CrossRef] [PubMed]

70. Nataf, G.F.; Guennou, M.; Gregg, J.M.; Meier, D.; Hlinka, J.; Salje, E.K.H.; Kreisel, J. Domain-wall engineering and topological defects in ferroelectric and ferroelastic materials. *Nat. Rev. Phys.* **2020**, *2*, 634–648. [CrossRef]
71. Salje, E.K.H.; Ding, X.; Zhao, Z.; Lookman, T.; Saxena, A. Thermally activated avalanches: Jamming and the progression of needle domains. *Phys. Rev. B* **2011**, *83*, 104109. [CrossRef]
72. Catalan, G.; Seidel, J.; Ramesh, R.; Scott, J.F. Domain wall nanoelectronics. *Rev. Mod. Phys.* **2012**, *84*, 119–156. [CrossRef]
73. Scott, J.J.; Lu, G.; Rodriguez, B.J.; MacLaren, I.; Salje, E.K.; Arredondo, M. Evidence of the Monopolar-Dipolar Crossover Regime: A Multiscale Study of Ferroelastic Domains by In Situ Microscopy Techniques. *Small* **2024**, *20*, 2400646. [CrossRef]
74. Dutta, D.P.; Jayakumar, O.D.; Tyagi, A.K.; Girija, K.G.; Pillai, C.G.S.; Sharma, G. Effect of doping on the morphology and multiferroic properties of $BiFeO_3$ nanorods. *Nanoscale* **2010**, *2*, 1149–1154. [CrossRef] [PubMed]
75. Morozovska, A.N.; Eliseev, E.A.; Glinchuk, M.D. Ferroelectricity enhancement in confined nanorods: Direct variational method. *Phys. Rev. B* **2006**, *73*, 214106. [CrossRef]
76. Watari, K.; Brahmaroutu, B.; Messing, G.L.; Trolier-McKinstry, S.; Cheng, S.C. Epitaxial growth of anisotropically shaped, single-crystal particles of cubic $SrTiO_3$. *J. Mater. Res.* **2000**, *15*, 846–849. [CrossRef]
77. Lu, G.M.; Ding, X.D.; Sun, J.; Salje, E.K.H. Wall-wall and kink-kink interactions in ferroelastic materials. *Phys. Rev. B* **2022**, *106*, 144105. [CrossRef]
78. Lu, G.M.; Salje, E.K.H. Multiferroic neuromorphic computation devices. *Appl. Phys. Lett. Mater.* **2024**, *12*, 061101. [CrossRef]
79. Salje, E.K.H.; Wang, X.F.; Ding, X.D.; Scott, J.F. Ultrafast Switching in Avalanche-Driven Ferroelectrics by Supersonic Kink Movements. *Adv. Funct. Mater.* **2017**, *27*, 1700367. [CrossRef]
80. Salje, E.K.H.; Dahmen, K.A. Crackling noise in disordered materials. *Ann. Rev. Condens. Matter Phys.* **2014**, *5*, 233–254. [CrossRef]
81. Salje, E.K.H.; Xue, D.; Ding, X.; Dahmen, K.A.; Scott, J.F. Ferroelectric switching and scale invariant avalanches in $BaTiO_3$. *Phys. Rev. Mater.* **2019**, *3*, 014415. [CrossRef]
82. Sethna, J.P.; Dahmen, K.A.; Myers, C.R. Crackling noise. *Nature* **2001**, *410*, 242–250. [CrossRef]
83. Tsai, S.T.; Wang, L.M.; Huang, P.P.; Yang, Z.N.; Chang, C.D.; Hong, T.M. Acoustic Emission from Breaking a Bamboo Chopstick. *Phys. Rev. Lett.* **2016**, *116*, 035501. [CrossRef]
84. Jiang, X.; Jiang, D.Y.; Chen, J.; Salje, E.K.H. Collapsing minerals: Crackling noise of sandstone and coal, and the predictability of mining accidents. *Am. Mineral.* **2016**, *101*, 2751–2758. [CrossRef]
85. Alava, M.J.; Nukalaz, P.K.V.V.; Zapperi, S. Statistical models of fracture. *Adv. Phys.* **2006**, *55*, 349–476. [CrossRef]
86. Bak, P.; Sneppen, K. Punctuateed equilibrium and criticality in a simple model of evolution. *Phys. Rev. Lett.* **1993**, *71*, 4083–4086. [CrossRef]
87. Eckstein, J.T.; Wiseman, O.J.; Carpenter, M.A.; Salje, E.K.H. Acoustic emission of kidney stones: A medical adaptation of statistical breakdown mechanisms. *Urolithiasi* **2024**, *52*, 36. [CrossRef]
88. Guglielmi, A.V. Omori's law: A note on the history of geophysics. *Phys. Usp.* **2017**, *60*, 319. [CrossRef]
89. Utsu, T. A statistical study on the occurrence of aftershocks. *Geophys. Mag.* **1961**, *30*, 521–605.
90. McGuire, J.J.; Boettcher, M.S.; Jordan, T.H. Foreshock sequences and short-term earthquake predictability on east pacific rise transform faults. *Nature* **2005**, *434*, 457–461. [CrossRef]
91. Alfvén, H. On the theory of the Barkhausen-Kurz oscillations. *Philos. Mag.* **1935**, *19*, 419–422. [CrossRef]
92. Wadley, H.N.G.; Mehrabian, R. Acoustic emission for materials processing: A review. *Mater. Sci. Eng.* **1984**, *65*, 245–263. [CrossRef]
93. Baró, J.; Corral, A.; Illa, X.; Planes, A.; Salje, E.K.H.; Schranz, W.; Soto-Parra, D.E.; Vives, E. Statistical Similarity between the Compression of a Porous Material and Earthquakes. *Phys. Rev. Lett.* **2013**, *110*, 088702. [CrossRef]
94. Dahmen, K.A.; Sethna, J.P. Hysteresis, avalanches, and disorder-induced critical scaling: A renormalization-group approach. *Phys. Rev. B* **1996**, *53*, 14872. [CrossRef] [PubMed]
95. Zaiser, M. Scale invariance in plastic flow of crystalline solids. *Adv. Phys.* **2006**, *55*, 185–245. [CrossRef]
96. Kustov, S.; Liubimova, I.; Salje, E.K.H. Domain Dynamics in Quantum-Paraelectric $SrTiO_3$. *Phys. Rev. Lett.* **2020**, *124*, 016801. [CrossRef] [PubMed]
97. Kleemann, W. Relaxor ferroelectrics: Cluster glass ground state via random fields and random bonds. *Phys. Status Solidi B* **2014**, *251*, 1993–2002. [CrossRef]
98. Lajzerowicz, J.J.; Levanyuk, A.P. Fluctuation-induced interaction of domain walls: Influence on the commensurate-incommensurate transition. *Phys. Rev. B* **1994**, *49*, 15475. [CrossRef]
99. Salje, E.K.H.; Iishibashi, Y. Mesoscopic structures in ferroelastic crystals: Needle twins and right-angled domains. *J. Phys. Condens. Matter* **1996**, *8*, 8477–8495. [CrossRef]
100. Lu, G.; Hideo, K.; Ding, X.; Chu, R.; Nataf, G.F.; Salje, E.K.H. Influence of kinks on the interaction energy between ferroelastic domain walls in membranes and thin films. *Microstructures* **2023**, *3*, 2023033. [CrossRef]
101. Salje, E.K.H.; Ding, X.; Aktas, O. Domain glass. *Phys. Status Solidi B* **2014**, *251*, 2061–2066. [CrossRef]
102. Cordero, F.; Trequattrini, F.; da Silva, P.S.; Venet, M.; Aktas, O.; Salje, E.K.H. Elastic precursor effects during $Ba_{1-x}Sr_xTiO_3$ ferroelastic phase transitions. *Phys. Rev. Research* **2023**, *5*, 013121. [CrossRef]
103. Ishibashi, Y.; Iwata, M. Activation Energy of Ferroelectric Domain Walls. *J. Phys. Soc. Jpn.* **2020**, *89*, 014705. [CrossRef]
104. Lu, G.M.; Cordero, F.; Hideo, K.; Ding, X.D.; Xu, Z.J.; Chu, R.Q.; Howard, C.J.; Carpenter, M.A.; Salje, E.K.H. Elastic precursor softening in proper ferroelastic materials: A molecular dynamics study. *Phys. Rev. Res.* **2014**, *6*, 013232. [CrossRef]

105. Pan, J.; Ivanov, Y.P.; Zhou, W.H.; Li, Y.; Greer, A.L. Strain-hardening and suppression of shear-banding in rejuvenated bulk metallic glass. *Nature* **2020**, *578*, 559–662. [CrossRef] [PubMed]
106. Rossetti, G.A.; Khachaturyan, A.G.; Akcay, G.; Ni, Y. Ferroelectric solid solutions with morphotropic boundaries: Vanishing polarization anisotropy, adaptive, polar glass, and two-phase states. *J. Appl. Phys.* **2008**, *103*, 114113. [CrossRef]
107. Monroe, J.A.; Raymond, J.E.; Xu, X.; Nagasako, M.; Kainuma, R.; Chumlyakov, Y.I.; Arroyave, R.; Karaman, I. Multiple ferroic glasses via ordering. *Acta Mater.* **2015**, *101*, 107–115. [CrossRef]
108. Bratkowsky, A.M.; Marais, S.C.; Heine, V.; Salje, E.K.H. The theory of fluctuations and texture embryos in structural phase-transitions mediated by strain. *J. Phys.-Condens. Matter* **1994**, *6*, 3679–3696. [CrossRef]
109. Rouxel, T. Elastic properties and short-to medium-range order in glasses. *J. Am. Ceram. Soc.* **2007**, *90*, 3019–3039. [CrossRef]
110. Kartha, S.; Krumhansl, J.A.; Sethna, J.P.; Wickam, L.K. Disorder-driven pretransitional tweed pattern in martensitic transformations. *Phys. Rev. B* **1995**, *52*, 803–822. [CrossRef]
111. Artemev, A.; Wang, Y.; Khachaturyan, A.G. Three-dimensional phase field model and simulation of martensitic transformation in multilayer systems under applied stress. *Acta Mater.* **2000**, *48*, 2503–2518. [CrossRef]
112. Kartha, S.; Castan, T.; Krumhansl, J.A.; Sethna, J.P. Spin-glass nature of tweed precursors in martensitic transformations. *Phys. Rev. Lett.* **1991**, *67*, 3630–3633. [CrossRef]
113. Naumov, I.; Bratkowsky, A.M. Unusual polarisation patterns in flat epitaxial ferroelectric nanoparticles. *Phys. Rev. Lett.* **2008**, *101*, 107601. [CrossRef]
114. Sandiumenge, F.; Rodríguez, L.; Pruneda, M.; Magén, C.; Santiso, J.; Catalan, G. Metallic Diluted Dimerization in VO_2 Tweeds. *Adv. Mater.* **2021**, *33*, 2004374. [CrossRef] [PubMed]